TECHNISCHE MECHANIK
an open access journal

journal homepage: www.ovgu.de/techmech

Tech. Mech., Vol. 40, Is. 1, (2020), 5–14

Received: 03.09.2019
Accepted: 10.11.2019
Available online: 15.02.2020

A Hybrid Approach to Describe the Elastic-Plastic Deformation Behavior of 2D Cellular Solids Including Damage Effects

Martin Abendroth[1]*, Geralf Hütter[1], Christoph Settgast[1], Alexander Malik[1], Björn Kiefer[1], and Meinhard Kuna[1]

[1] TU Bergakademie Freiberg, Institute of Mechanics and Fluiddynamics, Lampadiusstraße 4, 09599 Freiberg, Germany

Abstract: The constitutive description of the inelastic deformation behavior of porous media is a challenging task. The complex hardening behavior (simultaneous isotropic, kinematic and distortional hardening) and anisotropic yielding depend strongly on the micro-structure of the porous medium and the inelastic behavior of its bulk material.
In previous work, the authors presented a homogenized material model for an elastic-plastic material at the microscopic scale based on an adapted yield function to describe the elastic-plastic deformation behavior, including damage, of open-cell structures. In this approach, the shape of the yield function is not specified completely a priori. The proper shape is rather found by regression with results of cell model simulations using neural networks.
The aim of this contribution is to demonstrate that this hybrid approach shows good agreement with direct simulations. The necessary size of the neural network, the number of training data and the computational efficiency are also discussed. It can be concluded that this model can be used to analyze the deformation behavior of porous structures while considering the coupling of plastic deformations and damage of the bulk material.

Keywords: porous media, elastic-plastic deformation, damage, constitutive modeling, neural network

1 Introduction

Porous media have a wide range of application. This contribution was made within the framework of the DFG-Collaborative Research Center (CRC 920), where ceramic foams are investigated as filters for metal melt filtration applications (Emmel and Aneziris, 2012). Due to the very high application temperatures (1650°C for steel melt filtration) even the ceramic filters made of alumina (Al_2O_3) undergo inelastic deformations during loading (Solarek et al., 2016), which is why a constitutive material model is needed to simulate the mechanical behavior of such structures and to predict strength and deformation prior to an experiment.
But independent of the application, the macroscopic deformation behavior of porous media is complex and challenging, especially if homogenization approaches are considered. The micro-structure has a large influence on the shape of yield functions (Wang and McDowell, 2005), even if the bulk material is considered to be a *simple* material (Demiray et al., 2007; Storm et al., 2015), because isotropic, kinematic and distortional hardening can be observed.
To investigate the behavior of porous structures, representative volume elements (RVEs) of idealized periodic structures are often used to reduce the overall complexity. In many cases simple structures are chosen as RVEs, such as Kelvin cells, as done by (Demiray et al., 2007; Storm et al., 2015).
But in general each structure can have its own special yield surface and corresponding evolution, so that a homogenized constitutive material model is needed which is adaptable to changes of the RVE micro-structure and bulk material behavior. There are different approaches to tackle such problems. Models for direct simulations of complex structures have a very large number of degrees of freedom (DOF) and therefore require a large numerical effort. Also FE^2 approaches, where the solution of an RVE is applied for each local point of the porous component, are very expensive. On the other hand, phenomenological constitutive relations for specific micro-structures are hard to find.
In this contribution, an alternative approach is presented, in which neural networks (NN) are used to partially represent the constitutive relations, because of their adaptability to the given problem. (Liang and Chandrashekhara, 2008) and (Javadi and Rezania, 2009) used NNs as a constitutive model for the elastic behavior of elastomeric foams and for soils. (Abendroth and Kuna, 2006) used NNs as replacement for a material test procedure to identify material parameters for constitutive models. A behavior for a combined material (soils) was modeled using NNs by (Wojciechowski, 2011). (Hashash et al., 2004) implemented NNs including their derivatives for elastic-plastic material behavior to compute the consistent algorithmic material tangent. A cyclic plastic analysis considering kinematic and isotropic hardening using a NN based material law was presented by (Furukawa and Hoffman, 2004).
There exist a number of freely available codes for neural network applications, ranging from packages with rather basic functionality such as FFNET from (Wojciechowski, 2011), up to very complex solutions as Googles TensorFlow. For the problems discussed here FFNET is perfectly suited, since it allows to compute derivatives for single hidden layer networks and to export a trained network as FORTRAN code, which can be compiled together with a UMAT for the finite element code ABAQUS.
This contribution is based on previous approaches. In (Settgast et al., 2019a) NNs represent the inelastic stress strain relation directly. In (Settgast et al., 2018) a hybrid approach was presented, where NNs are used as an adaptable part of specific yield

* E-mail address: martin.abendroth@imfd.tu-freiberg.de doi: 10.24352/UB.OVGU-2020-008

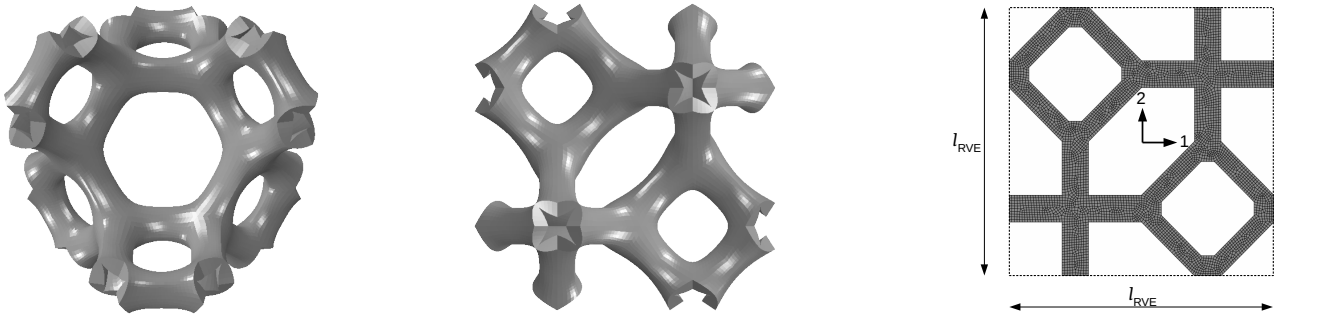

(a) <111>-view (b) <$\bar{1}$10>-view (c) Used 2D-RVE (relative density of $\varrho = 36.5\,\%$)

Fig. 1: From Kelvin-cell in 3D to used 2D-RVE as an idealized periodic structure.

surfaces, which was further improved by considering damage at the micro-scale in (Settgast et al., 2019b). In the present paper also practical issues are discussed, which include the necessary amount of training data, the structures and sizes of the neural networks with regard to the predictive accuracy of the model.

2 Homogenization

2.1 Microstructure and macroscopic values

A typical 3D structure used as RVE for an open cell foam is the Kelvin cell, see Fig. 1. To keep the effort for this work within limits, a simplified 2D structure, as depicted in Fig. 1(c), is used, which is derived from the Kelvin cell. It should be mentioned that the 2D projection of the Kelvin foam does not reflect the properties of the 3D Kelvin foam model, but serves as a proper model structure for the presented approach. The structure is periodic, whereas periodic boundary conditions

$$\boldsymbol{u} = \overline{\boldsymbol{\epsilon}} \cdot \boldsymbol{x} + \tilde{\boldsymbol{u}} \tag{1}$$

are applied to control the effective deformation $\overline{\boldsymbol{\epsilon}}$ in finite element simulations. Here, $\tilde{\boldsymbol{u}}$ denotes periodic fluctuations, which are equal at homologous points ($\boldsymbol{x}^-$ and $\boldsymbol{x}^+$) at the boundary of the RVE, i.e.

$$\tilde{\boldsymbol{u}}(\boldsymbol{x}^-) = \tilde{\boldsymbol{u}}(\boldsymbol{x}^+) \tag{2}$$

The periodic displacement fluctuations lead to the definition of equations for boundary nodes

$$\boldsymbol{u}(\boldsymbol{x}^+) - \boldsymbol{u}(\boldsymbol{x}^-) = \overline{\boldsymbol{\epsilon}} \cdot \left(\boldsymbol{x}^+ - \boldsymbol{x}^-\right). \tag{3}$$

Detailed information about the implementation of periodic boundary conditions and the corresponding homogenization theory can be found in (Storm et al., 2013).
Following Hill's homogenization theory, the macroscopic values for stress $\overline{\sigma}$, strain $\overline{\epsilon}$, and dissipation due to damage $\overline{D}$ are the volume weighted averages of the corresponding values at micro scale.

$$\overline{\boldsymbol{\sigma}} = \frac{1}{V_{\mathrm{RVE}}} \int_{V_{\mathrm{RVE}}} \boldsymbol{\sigma} \, \mathrm{d}V, \tag{4}$$

$$\overline{\boldsymbol{\epsilon}} = \frac{1}{V_{\mathrm{RVE}}} \int_{V_{\mathrm{RVE}}} \boldsymbol{\epsilon} \, \mathrm{d}V, \quad \text{and} \tag{5}$$

$$\overline{D} = \frac{1}{V_{\mathrm{RVE}}} \int_{V_{\mathrm{RVE}}} D \, \mathrm{d}V \tag{6}$$

2.2 Material model for the micro scale

The constitutive equations for the bulk material at the micro scale describe an elastic-plastic material with a Lemaitre-Kachanov-type damage formulation. The linear elastic behavior is defined by Hooke's law

$$\boldsymbol{\sigma} = \mathbb{C}^0 : \boldsymbol{\epsilon}^{\mathrm{el}} = \mathbb{C}^0 : \left(\boldsymbol{\epsilon} - \boldsymbol{\epsilon}^{\mathrm{pl}}\right), \tag{7}$$

where $\mathbb{C}^0$ denotes the isotropic stiffness tensor in the undamaged state defined with the elastic modulus E and Poisson's ratio $\nu = 0.14$. The ideally plastic behavior is described by a von Mises yield condition

$$\Phi(\boldsymbol{\sigma}) = \sigma_{\mathrm{eq}} - \sigma_{\mathrm{Y}} \tag{8}$$

with von Mises equivalent stress σ_{eq} and yield stress $\sigma_{\mathrm{Y}} = 0.061\,E = \text{const}$. Furthermore, an associated flow rule

$$\dot{\boldsymbol{\epsilon}}^{\mathrm{pl}} = \kappa \frac{\partial \Phi}{\partial \boldsymbol{\sigma}} \tag{9}$$

is assumed to hold, with the plastic multiplier κ. The loading-unloading conditions are equivalent to the Karush-Kuhn-Tucker conditions, which are

$$\Phi \leq 0, \quad \kappa \geq 0, \quad \Phi\,\kappa = 0. \tag{10}$$

The damage is considered to be isotropic, with a type damage variable D, which affects the stiffness tensor as

$$\boldsymbol{\sigma} = (1 - D)\,\mathbb{C}^0 \colon \left(\boldsymbol{\epsilon} - \boldsymbol{\epsilon}^{\mathrm{pl}}\right) \tag{11}$$

as well as the local yield stress

$$\Phi(\boldsymbol{\sigma}) = \sigma_{\mathrm{eq}} - (1 - D)\,\sigma_{\mathrm{Y}}. \tag{12}$$

The damage evolution is driven by the equivalent plastic strain rate

$$\dot{D} = \begin{cases} \frac{\sigma_{\mathrm{Y}} l_{\mathrm{element}}}{2\,G}\,\dot{\epsilon}^{\mathrm{pl}}_{\mathrm{eq}} & \text{if } \epsilon^{\mathrm{pl}}_{\mathrm{eq}} \geq \epsilon^{\mathrm{pl}_0}_{\mathrm{eq}} \\ 0 & \text{else} \end{cases} \tag{13}$$

and controlled by the constants for the finite element size $l_{\mathrm{element}} = 0.01\,l_{\mathrm{RVE}}$, the RVE size $l_{\mathrm{RVE}} = 1\,\mathrm{mm}$, a material constant $G = 150\,\sigma_{\mathrm{Y}}^2 l_{\mathrm{element}}/E$, and the threshold of the equivalent plastic strain $\epsilon^{\mathrm{pl}_0}_{\mathrm{eq}} = 0$, above which damage occurs.

3 Constitutive modeling using neural networks

3.1 Neural network

All functionalities based on neural networks are realized using the `python` library `ffnet` of (Wojciechowski, 2011), which provides tools to create, train and use feed-forward neural networks (FFNN). All networks used in this work have a similar structure. There is an input layer with n neurons, a single hidden layer having m neurons, and an output layer with k neurons as depicted in Fig. 2. The neurons of the hidden and output layers have a sigmoid activation function

$$h(v_j) = \frac{1}{1 + \exp(-v_j)}, \tag{14}$$

with v_j as nodal input value, representing the sum of the weighted activations $w_l h_l$ of the preceding layer, plus a bias b_j for each neuron j:

$$v_j = \sum_l w_l h_l + b_j. \tag{15}$$

The free parameters of such a network are the $n \cdot m + m \cdot k$ weights and $m + k$ biases, which are adjusted to the given problem by a training procedure. The training procedure minimizes the cost function for a training data set $\mathscr{D}_{\mathcal{T}}$:

$$err^{\mathrm{train}} = \frac{1}{2} \sum_{p \in \mathscr{D}_{\mathcal{T}}} \sum_k \left[val_k^{(p)} - \mathrm{NN}_k \left(inp^{(p)} \right) \right]^2, \tag{16}$$

using a truncated Newton method with normalized inputs $inp^{(p)}$ and outputs $out^{(p)} = \mathrm{NN}(inp^{(p)})$ data. The training data set $\mathscr{D}_{\mathcal{T}}$ is a subset of all data $\mathscr{D}_{\mathcal{D}}$, which also contains a validation data set $\mathscr{D}_{\mathcal{V}}$ representing another subset of size α of all data. Validation data however, are not part of the training data set.

$$\mathscr{D}_{\mathcal{T}} \cup \mathscr{D}_{\mathcal{V}} = \mathscr{D}_{\mathcal{D}} \tag{17}$$

$$\mathscr{D}_{\mathcal{T}} \cap \mathscr{D}_{\mathcal{V}} = \varnothing \tag{18}$$

$$|\mathscr{D}_{\mathcal{V}}| = \alpha\,|\mathscr{D}_{\mathcal{D}}| \quad \text{with} \quad 0 < \alpha < 1 \tag{19}$$

Prior to training, all values for weights and biases are set to random values in the range $[-b, b]$, where $b = 2.38/\sqrt{n}$ depends on the number n of incoming weights to a neuron.

3.2 Hybrid approach

This section explains the constitutive relations for the hybrid approach. The elastic response on the macro scale follows Hooke's law

$$\overline{\boldsymbol{\sigma}} = \overline{\mathbb{C}} \colon \left(\overline{\boldsymbol{\epsilon}} - \overline{\boldsymbol{\epsilon}}^{\mathrm{pl}}\right). \tag{20}$$

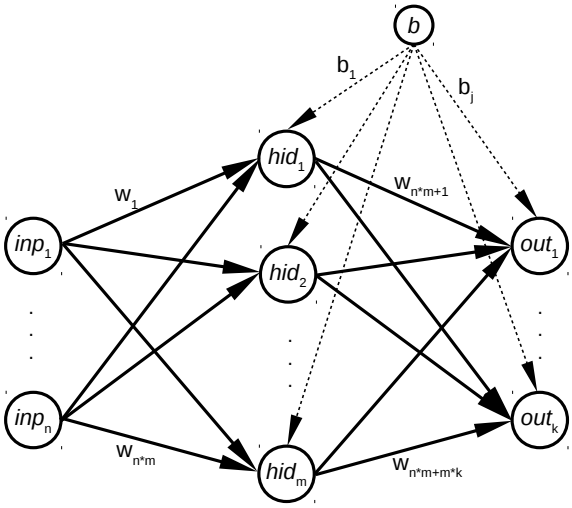

Fig. 2: Structure of the used neural networks (input layer with n neurons, one hidden layer with m neurons and output layer with k neurons, $n \cdot m + m \cdot k$ different weights $\boldsymbol{w}$ are applied at solid arrows and $m + k$ different biases $\boldsymbol{b}$ at dashed arrows).

The components of the effective stiffness tensor $\overline{\mathbb{C}}$ are obtained by three linearly independent load cases for 2D problems or six load cases for 3D problems as described in detail in (Storm et al., 2013). The Helmholtz free energy is assumed in the form

$$\overline{\Psi} = \frac{1}{2}\left(\overline{\boldsymbol{\epsilon}} - \overline{\boldsymbol{\epsilon}}^{\mathrm{pl}}\right) \boldsymbol{:} \overline{\mathbb{C}} \boldsymbol{:} \left(\overline{\boldsymbol{\epsilon}} - \overline{\boldsymbol{\epsilon}}^{\mathrm{pl}}\right). \tag{21}$$

The yield function is adaptable, which means a specific shape is not a priori set. More specifically, it is assumed:

$$\overline{\Phi}^{\mathrm{NN}} = \hat{\overline{\sigma}} - \mathrm{NN}^{\hat{\overline{\sigma}}}(\overline{\epsilon}^{\mathrm{pl}}_{\mathrm{eq}}, \overline{I}^{\epsilon}_1, \left|\overline{\epsilon}^{\mathrm{pl}}_{12}\right|). \tag{22}$$

Here $\hat{\overline{\sigma}} := \|\overline{\boldsymbol{\sigma}}\| = \sqrt{\overline{\boldsymbol{\sigma}} \boldsymbol{:} \overline{\boldsymbol{\sigma}}}$ and $\mathrm{NN}^{\hat{\overline{\sigma}}}(\overline{\epsilon}^{\mathrm{pl}}_{\mathrm{eq}}, \overline{I}^{\epsilon}_1, \left|\overline{\epsilon}^{\mathrm{pl}}_{12}\right|)$ denotes a neural network function having effective equivalent plastic strain $\overline{\epsilon}^{\mathrm{pl}}_{\mathrm{eq}}$, the volumetric plastic strain $\overline{I}^{\epsilon}_1$ and the absolute shear strain $\left|\overline{\epsilon}^{\mathrm{pl}}_{12}\right|$ as arguments to consider isotropic, distortional and volumetric hardening. For a three dimensional case, or other porous structures, the arguments (inputs) for neural networks may be chosen differently. Suitable inputs can be the invariants of effective stress or strain tensors, angles in strain space as well as additional internal variables which characterize the deformation state of the RVE. For highly porous materials, a non-associated flow rule is appropriate

$$\dot{\overline{\boldsymbol{\epsilon}}}^{\mathrm{pl}} = \dot{\overline{\kappa}} \overline{\boldsymbol{N}}^{\mathrm{pl}} = \dot{\overline{\epsilon}}^{\mathrm{pl}}_{\mathrm{eq}} \underbrace{\frac{\overline{\boldsymbol{N}}^{\mathrm{pl}}}{\|\overline{\boldsymbol{N}}^{\mathrm{pl}}\|}}_{\check{\overline{\boldsymbol{N}}}^{\mathrm{pl}}}, \tag{23}$$

with the normalized flow direction

$$\check{\overline{\boldsymbol{N}}}^{\mathrm{pl}} = \frac{1}{2}\left(\sin\overline{\alpha}_{\overline{\pi}} + \cos\overline{\alpha}_{\overline{\pi}}\right)\boldsymbol{I} + \frac{1}{2}\left(\cos\overline{\alpha}_{\overline{\pi}} - \sin\overline{\alpha}_{\overline{\pi}}\right)\frac{\overline{\boldsymbol{s}}}{\sqrt{J_2^{\overline{\boldsymbol{\sigma}}}}}, \tag{24}$$

which is composed of a spherical and deviatoric part. Here, $\boldsymbol{I}$ denotes the unit tensor, $\overline{\boldsymbol{s}}$ the deviatoric stress and $J_2^{\overline{\boldsymbol{\sigma}}}$ the second stress invariant. The ratio of spherical and deviatoric parts is expressed by a second neural network, also with the same general set of arguments $\overline{\epsilon}^{\mathrm{pl}}_{\mathrm{eq}}$, $\overline{I}^{\epsilon}_1$ and $\left|\overline{\epsilon}^{\mathrm{pl}}_{12}\right|$.

$$\overline{\alpha}_{\overline{\pi}} = \mathrm{NN}^{\check{\overline{N}}}(\overline{\epsilon}^{\mathrm{pl}}_{\mathrm{eq}}, \overline{I}^{\epsilon}_1, \left|\overline{\epsilon}^{\mathrm{pl}}_{12}\right|) \tag{25}$$

In equation (24) it is assumed that the principle axes of stress and plastic flow coincide (Settgast et al., 2019b). The principle structure of all networks is similar to that indicated in Fig. 2. They differ only in the number of neurons in the hidden and output layers.

3.3 Extension for damage

The damage evolution at the macro-scale is assumed to be anisotropic, although it is modeled isotropically at the micro-scale. $\overline{\mathbb{C}}$ is considered as an internal state variable and its changes are described using a third neural network

$$\dot{\overline{\mathbb{C}}} = \dot{\overline{\epsilon}}^{\mathrm{pl}}_{\mathrm{eq}}\, \mathbf{NN}^{\dot{\overline{\mathbb{C}}}}(\overline{\epsilon}^{\mathrm{pl}}_{\mathrm{eq}}, \overline{I}^{\epsilon}_1, \left|\overline{\epsilon}^{\mathrm{pl}}_{12}\right|), \tag{26}$$

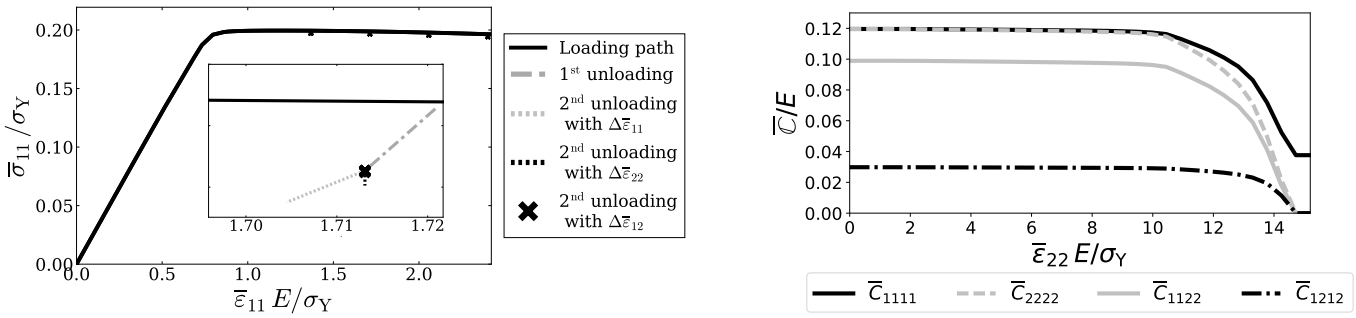

Fig. 3: One specific loading path with unloading steps for the extraction of the coefficients of the effective stiffness tensor $\overline{\mathbb{C}}$ (left) and the evolution of the coefficients of $\overline{\mathbb{C}}$ for uniaxial stretching in 2-direction (right).

with same arguments as the other two. Consequently, the dissipation equation of the model takes the form:

$$\dot{\overline{D}} = \overline{\boldsymbol{\sigma}} : \dot{\overline{\boldsymbol{\epsilon}}}^{\mathrm{pl}} - \frac{\partial \overline{\Psi}}{\partial \overline{\mathbb{C}}} :: \dot{\overline{\mathbb{C}}} = \overline{\boldsymbol{\sigma}} : \dot{\overline{\boldsymbol{\epsilon}}}^{\mathrm{pl}} - \frac{1}{2} \left(\overline{\boldsymbol{\epsilon}} - \overline{\boldsymbol{\epsilon}}^{\mathrm{pl}} \right) : \mathbf{N}\mathbf{N}^{\dot{\overline{\mathbb{C}}}} (\overline{\epsilon}^{\mathrm{pl}}_{\mathrm{eq}}, \overline{I}^{\epsilon}_1, \left| \overline{\epsilon}^{\mathrm{pl}}_{12} \right|) : \left(\overline{\boldsymbol{\epsilon}} - \overline{\boldsymbol{\epsilon}}^{\mathrm{pl}} \right) \dot{\overline{\epsilon}}^{\mathrm{pl}}_{\mathrm{eq}}. \tag{27}$$

It should be noted that $\dot{\overline{D}} \geq 0$ is not a priori guaranteed from the macroscopic model. However, the training data are, in this case, obtained from a thermodynamically consistent model. Nevertheless, the values of $\dot{\overline{D}}$ are checked during the evaluation of the homogenized material model.

3.4 Generation of training data for the neural networks

To generate all data $\mathscr{D}_{\mathcal{D}}$, a number of RVE simulations are performed. To this end, proportional load paths

$$\overline{\boldsymbol{\epsilon}} = \lambda \, \overline{\boldsymbol{\epsilon}}^{*} \tag{28}$$

are defined, with $\lambda \in \mathscr{R}^{+}_{0}$ and $\lambda = 1$ for initial yielding at the micro-scale. For proportional load paths, only isotropic and distortional hardening can be evaluated. To catch kinematic hardening, non-proportional load paths with checks for yielding at the micro-scale would be necessary. For the 2D structure depicted in Fig. 1(c), the load path in strain space is defined using two angles ϕ and ψ, i.e.

$$\overline{\boldsymbol{\epsilon}} = \boldsymbol{R}^{T} \boldsymbol{A} \boldsymbol{R} \quad \text{with} \quad \boldsymbol{A} = \begin{bmatrix} \cos\phi & 0 \\ 0 & \sin\phi \end{bmatrix} \quad \text{and} \quad \boldsymbol{R} = \begin{bmatrix} \cos\psi & -\sin\psi \\ \sin\psi & \cos\psi \end{bmatrix}, \tag{29}$$

rastered with $\Delta\phi = \Delta\psi$. The step sizes $\Delta\phi$, $\Delta\psi$ and $\Delta\lambda$ define the number of data points available for training and validation. For each load increment, effective stress $\overline{\boldsymbol{\sigma}}$ and strain $\overline{\boldsymbol{\epsilon}}$ are determined and it is checked whether local yielding occurs. If yielding happens at the micro-scale, then $\overline{\Phi} = 0$ and the corresponding stress $\overline{\boldsymbol{\sigma}}$ and the input data ϕ, ψ and $\overline{\epsilon}^{\mathrm{pl}}_{\mathrm{eq}}$ are appended to a data set which is used to train the network $\mathrm{NN}^{\|\overline{\boldsymbol{\sigma}}\|}$. The choice of ϕ and ψ as input data is motivated by the fact that it contains equivalent information about the strain direction as $\overline{I}^{\epsilon}_1$ and $\left|\overline{\epsilon}^{\mathrm{pl}}_{12}\right|$. The plastic strain is determined using

$$\overline{\boldsymbol{\epsilon}}^{\mathrm{pl}} = \overline{\boldsymbol{\epsilon}} - \overline{\mathbb{C}}^{-1} : \overline{\boldsymbol{\sigma}}, \tag{30}$$

which is further used to compute the flow direction

$$\overline{\boldsymbol{N}}^{\mathrm{pl}} := \frac{\dot{\overline{\boldsymbol{\epsilon}}}^{\mathrm{pl}}}{\dot{\overline{\epsilon}}^{\mathrm{pl}}_{\mathrm{eq}}}. \tag{31}$$

In Eqn. (30), the actual stiffness tensor is required. Therefore, a partial unloading of the RVE is simulated, making sure that its stress state falls within the elastic limit. From this state $\overline{\boldsymbol{\epsilon}}^{(0)}$, three additional load cases with load increments $\Delta\overline{\boldsymbol{\epsilon}}^{(1)} = [\epsilon_0, 0, 0]$, $\Delta\overline{\boldsymbol{\epsilon}}^{(2)} = [0, \epsilon_0, 0]$, and $\Delta\overline{\boldsymbol{\epsilon}}^{(3)} = [0, 0, \epsilon_0]$ are simulated. From the resulting stress increments $\Delta\overline{\boldsymbol{\sigma}}^{(i)}$ all coefficients of the stiffness tensor can be determined using

$$\overline{\mathbb{C}}_{i1} = \frac{\Delta\overline{\boldsymbol{\sigma}}^{(1)}}{\epsilon_0}, \quad \overline{\mathbb{C}}_{i2} = \frac{\Delta\overline{\boldsymbol{\sigma}}^{(2)}}{\epsilon_0}, \quad \overline{\mathbb{C}}_{i3} = \frac{\Delta\overline{\boldsymbol{\sigma}}^{(3)}}{\epsilon_0}, \quad i \in [1, 2, 3]. \tag{32}$$

Also, ϵ_0 is chosen here such that the resulting stress state is inside the elastic limit. The procedure to extract values of $\overline{\mathbb{C}}$ and the resulting coefficients for a single loading path are shown in Fig. 3, which also indicates the evolving anisotropy of the RVE if damage is considered at the micro-scale. A schematic representation of the whole procedure to generate data for neural network training is shown in Fig. 4.

In this case, the entire data set used for training and validation $\mathscr{D}_{\mathcal{D}}$ is generated using $\Delta\phi = \Delta\psi = 10°$ and $\Delta\lambda = 0.1$ for the ranges $\phi \in [0°, 180°]$, $\psi \in [0°, 90°]$ and $\lambda \in [1, 10]$, resulting in 32400 samples.

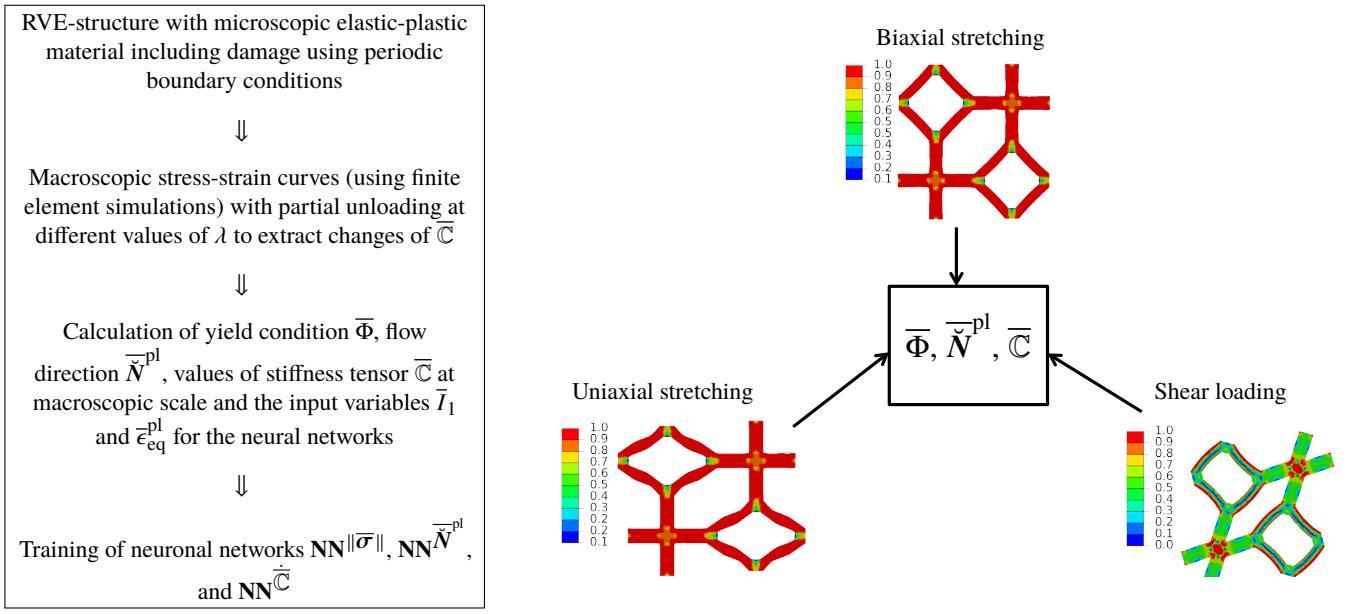

Fig. 4: Steps involved in the generation of the neural networks for the description of the elastic-plastic deformation behavior and damage at the microscopic scale of porous structures, illustrated for the discussed idealized 2D cellular structures.

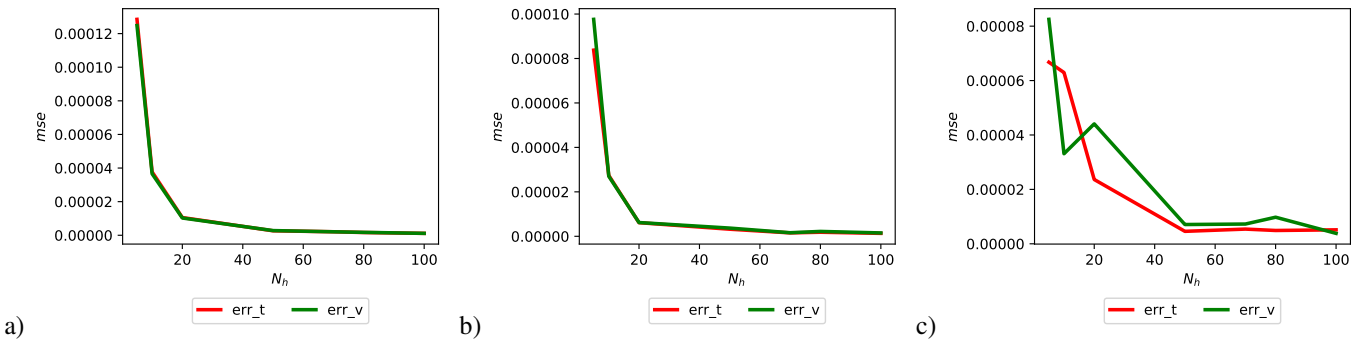

Fig. 5: Errors after training depending on the number of neurons in the hidden layer: a) for $\mathbf{NN}^{\|\overline{\boldsymbol{\sigma}}\|}$, b) for $\mathbf{NN}^{\overline{\check{N}}^{\mathrm{pl}}}$, c) for $\mathbf{NN}^{\dot{\overline{\mathbb{C}}}}$.

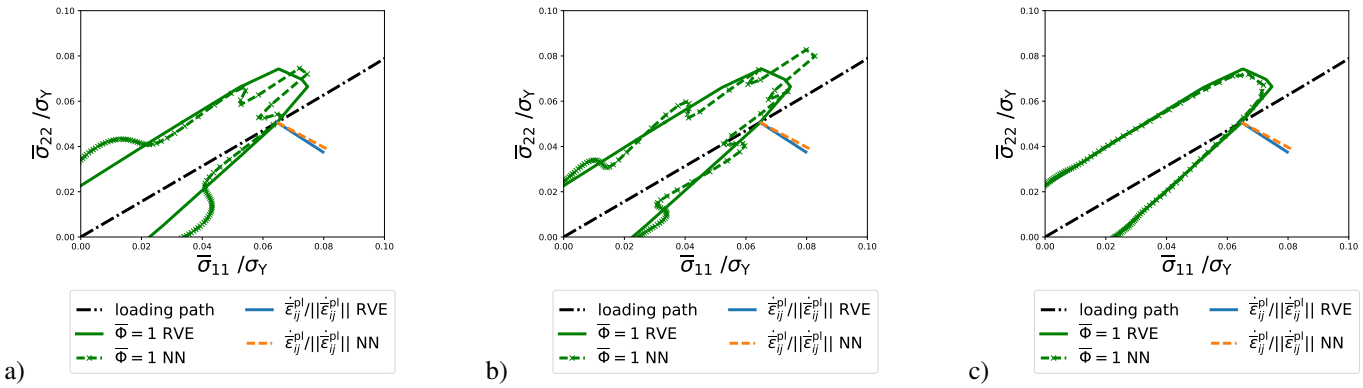

Fig. 6: Approximation quality for the initial yield surface and a loading direction depending on the number neurons in the hidden layer: a) 20, b) 50 and c) 80 neurons.

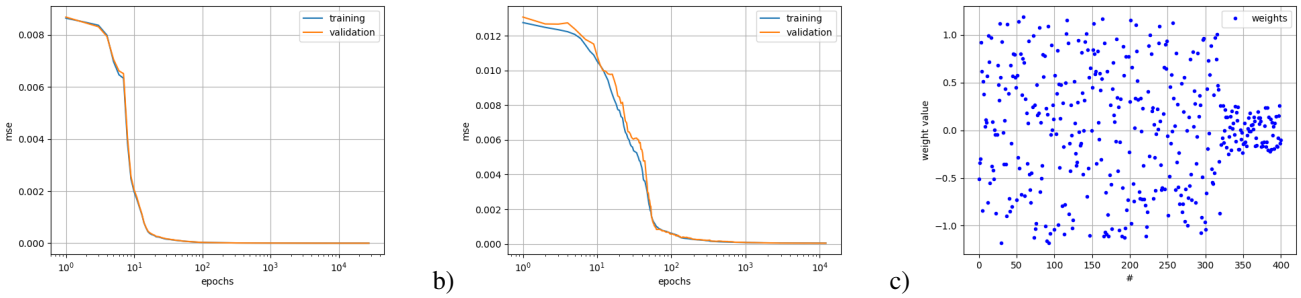

a) b) c)

Fig. 7: Error evolution for training and validation data: a) for $\mathbf{NN}^{\|\overline{\boldsymbol{\sigma}}\|}$, b) for $\mathbf{NN}^{\overline{\tilde{N}}^{\mathrm{pl}}}$., whereas c) shows the distribution of weight values for $\mathbf{NN}^{\|\overline{\boldsymbol{\sigma}}\|}$.

3.5 Accuracy and numerical effort

The accuracy of a trained NN crucially depends on the number of neurons N_{h} within the network. It should be large enough to represent the complexity of the problem, but small enough to avoid , which is indicated by an increasing error for validation data for an increasing number of neurons. For the present study, the number of neurons within the hidden layer was varied between 5 and 100. Fig. 5 shows the mean square error as a function of the number of hidden neurons for the three different networks after training. It is evident that for the specific problem a number of 80 hidden neurons is a good choice for $\mathbf{NN}^{\|\overline{\boldsymbol{\sigma}}\|}$ and $\mathbf{NN}^{\overline{\tilde{N}}^{\mathrm{pl}}}$, whereas 50 hidden neurons are sufficient for $\mathbf{NN}^{\dot{\overline{\mathbb{C}}}}$. The mean square error after training for all networks is around $5 \cdot 10^{-6}$, which corresponds to an absolute error of $\approx 0.2\%$.
Fig. 6 shows the neural network prediction of the initial yield surface. Here it becomes clear that a sufficient number of neurons is necessary to approximate the yield surfaces with a certain accuracy. For a small number of neurons in the neural network, fluctuations in the network function are observed, even though the mean square error after completion of training is very small. This behavior is most likely connected to the sampling strategy, which must be discussed. If the training samples are arranged in a regular grid as it is done here, the network function can show periodic fluctuations. This could potentially be reduced if a latin hypercube sampling (LHS) strategy would be used. The LHS strategy subdivides the sample space into equally-sized hypercubes. Within each hypercube, a certain number of samples is generated randomly. The randomness reduces periodic fluctuations.
Another sign for potential inaccuracies, which was not observed here (see Fig. 7), is a small number of weights having unusual large values, which can lead to spikes in the network function in regions where no training data are present. In such cases, modifications of the training algorithm can be useful, where the cost function penalizes weight outliers within the training algorithm.
One of the most interesting questions is how many training data are necessary to achieve a certain approximation accuracy of the NN. In Fig. 8 the approximation accuracy is compared for networks which were trained with the full data set sampled with $\Delta\phi = \Delta\psi = 10°$ and for networks trained with a data sampled with $\Delta\phi = 30°$ and $\Delta\psi = 10°$. Although the smaller data set contained just one third of all data, the approximation accuracy remains almost constant. But a further reduction of training data decreases the approximation quality drastically.
The main numerical effort associated with this approach is the generation of training samples, which requires a large number of finite element simulations of the RVE. For the given example, all simulations required approximately 10^5 CPU (2.8 GHz) seconds. The much smaller effort lies in the training of the neural networks which naturally depends on the number of training samples, the network size and the number of training epochs and certainly on the training algorithm. For the given problem the truncated Newton algorithm is suitable. The training for a small benchmark problem with 8000 data samples, a 3-50-1 network, 1000 training epochs on a single 2.8 GHz processor took approximately 20 seconds. As a rule of thumb for such rather small problems, the time for network training scales linearly with the number of training data, number of weights, number of samples and number of training epochs.

4 Application for a single RVE

To evaluate the performance of the constitutive modeling approach using neural networks, we compare the results of the model with those of the fully-meshed RVE, as shown in Fig. 1c. All the networks used for this purpose had 80 neurons within the hidden layer.

4.1 Partial unloading

In a first example, no damage is considered, which means that the effective stiffness tensor remains constant $\overline{\mathbb{C}} = \overline{\mathbb{C}}^0$ and no neural network is needed for the evolution of $\overline{\mathbb{C}}$ described in Eqn. (26). Three different loading paths with partial unloading are applied, both to the model and the RVE. In Fig. 8 the responses are compared for a) uniaxial extension in 1-direction, b) isochoric deformation without shear, and c) biaxial strain without shear. For all three cases, one observes a very good agreement between the effective responses of the RVE and the predictions of the model. The time to evaluate a single load path using the fully-meshed RVE is about 250 seconds, compared to 5 seconds for the homogenized model, which corresponds to a speed up factor of 50.

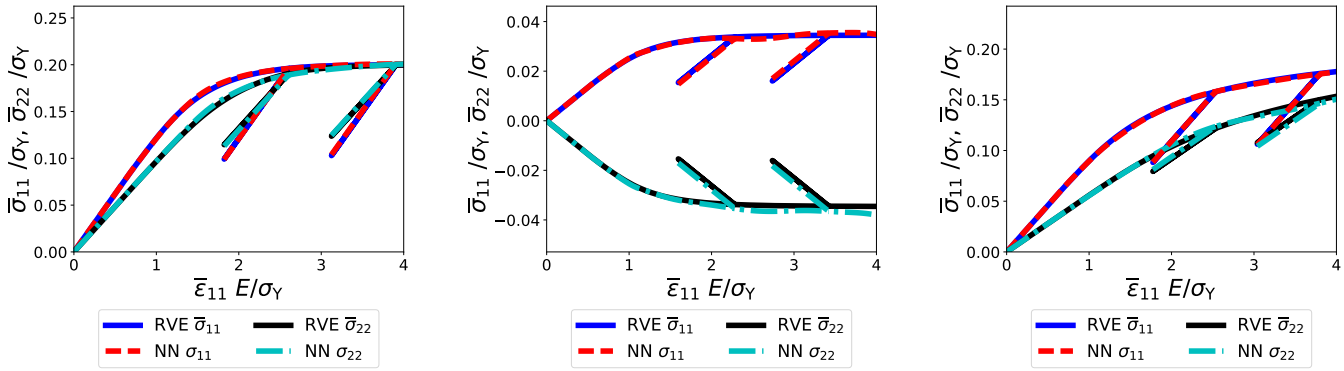

(a) $\Delta\phi = \Delta\psi = 10°$, $\overline{\epsilon}_{22} = 0$, $\overline{\epsilon}_{12} = 0$ (b) $\Delta\phi = \Delta\psi = 10°$, $\overline{\epsilon}_{22} = -\overline{\epsilon}_{11}$, $\overline{\epsilon}_{12} = 0$ (c) $\Delta\phi = \Delta\psi = 10°$, $\overline{\epsilon}_{22} = \frac{1}{3}\overline{\epsilon}_{11}$, $\overline{\epsilon}_{12} = 0$

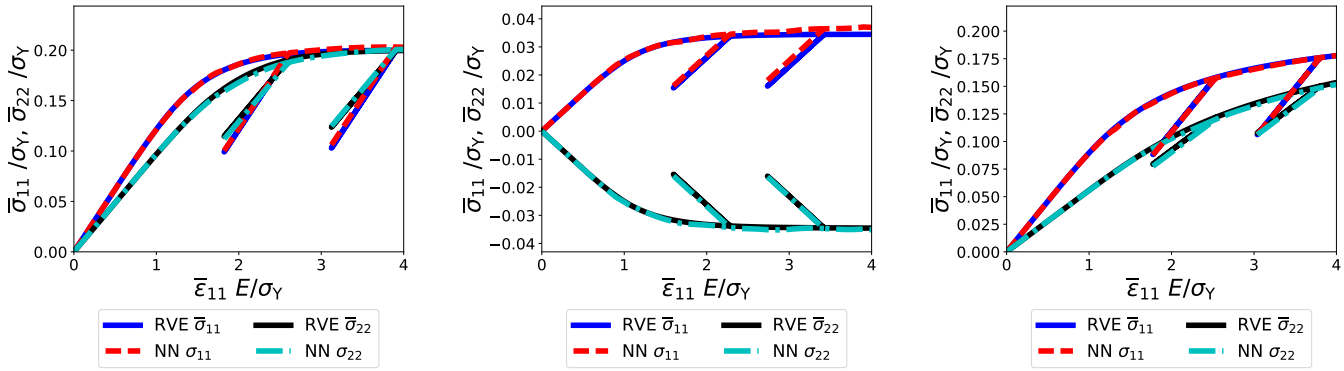

(d) $\Delta\phi = 30°$, $\Delta\psi = 10°$, $\overline{\epsilon}_{22} = 0$, $\overline{\epsilon}_{12} = 0$ (e) $\Delta\phi = 30°$, $\Delta\psi = 10°$, $\overline{\epsilon}_{22} = -\overline{\epsilon}_{11}$, $\overline{\epsilon}_{12} = 0$ (f) $\Delta\phi = 30°$, $\Delta\psi = 10°$, $\overline{\epsilon}_{22} = \frac{1}{3}\overline{\epsilon}_{11}$, $\overline{\epsilon}_{12} = 0$

Fig. 8: Stress-strain curves of three different proportional loading cases with partial unloading of RVE-simulations (RVE) and hybrid material model (NN) using elastic-plastic material without damage at microscopic scale from (Settgast et al., 2019b). First row shows results obtained with a NN, which was trained using data sampled with $\Delta\phi = \Delta\psi = 10°$, whereas in the second row the NN was trained with data sampled with $\Delta\phi = 30°$ and $\Delta\psi = 10°$.

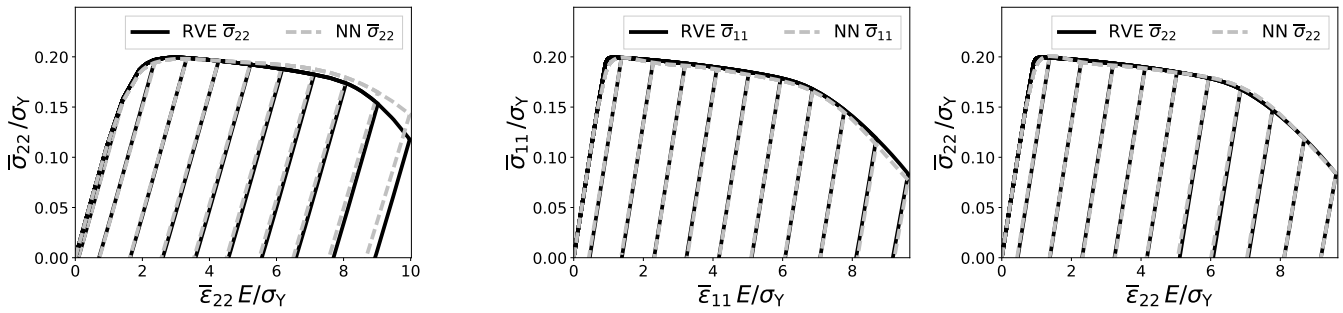

(a) uniaxial loading $\overline{\epsilon}_{22}$ (b) biaxial loading $\overline{\epsilon}_{11} = \overline{\epsilon}_{22}$

Fig. 9: Macroscopic stress-strain curves for different load cases, where damage is considered (Settgast et al., 2019b).

4.2 Damage at microscopic scale

In the second example damage is considered, which means that the effective stiffness tensor $\overline{\mathbb{C}}$ changes according to Eq. (26), leading to a decreasing load bearing capacity of the RVE with increasing plastic deformation. In Fig. 9, the response of the RVE is compared with the predictions of the NN model for two different load cases: a) an uniaxial loading, as well as b) a biaxial loading. In both cases, several loading-unloading stages are simulated. It is evident that the slope of the unloading curves decreases with increasing damage, due to the decrease in effective stiffness. The overall agreement between the predictions of the NN model and the direct RVE response is very satisfactory. The small differences, especially in the uniaxial case, are due to small approximation errors regarding $|\overline{\sigma}|$. The even smaller deviations in the biaxial load case are due to approximation errors regarding the flow direction $\overline{\breve{N}}^{\mathrm{pl}}$. It should be mentioned that periodic boundary conditions may overconstrain the localized deformation modes after onset of softening. Other types of less constraining BCs could be used for the generation of training data within the present approach without any problem. Though, this lies beyond the scope of the present manuscript.

5 Conclusions

In this contribution, it was demonstrated that neural networks can be used in constitutive models for porous media, to approximate yield surfaces, the plastic flow direction, and the evolution of damage. For this purpose, training data are needed, which are, for instance, obtained from finite element simulations of RVEs. In the current approach the training data are obtained from proportional load cases, where effective strains are defined. The model predictions were compared with results from direct simulations of the fully-meshed porous structure and show a very satisfactory accuracy. The influence of the neural network size, the data sampling strategy and the training algorithm were also discussed. It was concluded that especially the sampling strategy could be improved to avoid fluctuations of the neural network function. For the tested example, the evaluation of the hybrid model works approximately fifty times faster than the evaluation of the fully-meshed RVE. For three dimensional models, it is expected that the possible speed up increases even further.

It would be also possible to use experimental data instead of numerically generated ones, if a sufficiently elaborate data set were available. For a general application, it is necessary to extend this approach to three dimensions, which is mathematically straightforward, because the set of equations does not change. However, the computational effort to generate a sufficiently large set of data increases, because the RVE has to be three-dimensional and the number of loading direction paths has to be adapted accordingly.

On the other hand no constitutive model currently exists, which is capable of simulating arbitrary porous structures. The presented approach can be applied for structures where the principle shape of their yield and flow potentials is unknown or very difficult to formulate in closed-form.

Finally, useful extensions should consider more internal variables (e.g. volumetric strain, data of internal distortional deformations, a.o.) for the input of the neural networks to increase their predictive accuracy.

Acknowledgment

The authors gratefully acknowledge the financial support by the German Research Foundation (DFG) within the collaborative research center SFB 920 „Multi-Functional Filters for Metal Melt Filtration – A Contribution towards Zero Defect Materials“ (DFG-169148856).

References

Martin Abendroth and Meinhard Kuna. Identification of ductile damage and fracture parameters from the small punch test using neural networks. *Engineering Fracture Mechanics*, 73(6):710–725, 2006. doi: 10.1016/j.engfracmech.2005.10.007.

Serkan Demiray, Wilfried Becker, and Jörg Hohe. Numerical determination of initial and subsequent yield surfaces of open-celled model foams. *International Journal of Solids and Structures*, 44(7):2093–2108, 2007. doi: 10.1016/j.ijsolstr.2006.06.044.

Marcus Emmel and Christos G Aneziris. Development of novel carbon bonded filter compositions for steel melt filtration. *Ceramics International*, 38(6):5165–5173, 2012. doi: 10.1016/j.ceramint.2012.03.022.

Tomonari Furukawa and Mark Hoffman. Accurate cyclic plastic analysis using a neural network material model. *Engineering Analysis with Boundary Elements*, 28(3):195–204, 2004. doi: 10.1016/S0955-7997(03)00050-X.

Youssef M.A. Hashash, Sungmoon Jung, and Jamshid Ghaboussi. Numerical implementation of a neural network based material model in finite element analysis. *International Journal for Numerical Methods in Engineering*, 59(7):989–1005, 2004. doi: 10.1002/nme.905.

Akbar A. Javadi and Mohammad Rezania. Intelligent finite element method: An evolutionary approach to constitutive modeling. *Advanced Engineering Informatics*, 23(4):442–451, 2009. doi: 10.1016/j.aei.2009.06.008.

Guanghui Liang and K. Chandrashekhara. Neural network based constitutive model for elastomeric foams. *Engineering Structures*, 30(7):2002–2011, 2008. doi: 10.1016/j.engstruct.2007.12.021.

Christoph Settgast, Geralf Hütter, Martin Abendroth, and Meinhard Kuna. A hybrid approach for consideration of the elastic-plastic behaviour of open-cell ceramic foams. In *Proceedings of the ECCM6/ECFD7, 11-15 June 2018, Glasgow, United Kingdom*, pages 2314–2325, 2018.

Christoph Settgast, Martin Abendroth, and Meinhard Kuna. Constitutive modeling of plastic deformation behavior of open-cell foam structures using neural networks. *Mechanics of Materials*, 131:1–10, 2019a. ISSN 0167-6636. doi: 10.1016/j.mechmat.2019.01.015.

Christoph Settgast, Geralf Hütter, Meinhard Kuna, and Martin Abendroth. A hybrid approach to simulate the homogenized irreversible elastic-plastic deformations and damage of foams by neural networks, 2019b.

Johannes Solarek, Christina Bachmann, Yvonne Klemm, Christos G. Aneziris, and Horst Biermann. High-temperature compression deformation behavior of fine-grained carbon-bonded alumina. *Journal of the American Ceramic Society*, 99(4):1390–1397, 4 2016. doi: 10.1111/jace.14070.

Johannes Storm, Martin Abendroth, Dongshuang Zhang, and Meinhard Kuna. Geometry dependent effective elastic properties of open-cell foams based on kelvin cell models. *Advanced Engineering Materials*, 15(12):1292–1298, 2013. doi: 10.1002/adem.201300141.

Johannes Storm, Martin Abendroth, and Meinhard Kuna. Numerical and analytical solutions for anisotropic yield surfaces of the open-cell Kelvin foam. *International Journal of Mechanical Sciences*, 105:70–82, 2015. doi: 10.1016/j.ijmecsci.2015.10.014.

Aijun Wang and David L. McDowell. Yield surfaces of various periodic metal honeycombs at intermediate relative density. *International Journal of Plasticity*, 21(2):285–320, 2005. doi: 10.1016/j.ijplas.2003.12.002.

Marek Wojciechowski. Application of artificial neural network in soil parameter identification for deep excavation numerical model. *Computer Assisted Mechanics and Engineering Sciences*, 18(4):303–311, 2011.